 CMES, vol.97, no.1, pp.53-80, 2014

Axisymmetric and 3-D Numerical Simulations of the Effects of a Static Magnetic Field on Dissolution of Silicon into Germanium

F. Mechighel[1,2,3], N. Armour[4], S. Dost[4] and M. Kadja[3]

Abstract: Numerical simulations were carried out to explain the behavior exhibited in experimental work on the dissolution process of silicon into a germanium melt. The experimental work utilized a material configuration similar to that used in the Liquid Phase Diffusion (LPD) and Melt-Replenishment Czochralski (Cz) growth systems. The experimental dissolution system was modeled by considering axisymmetric and three-dimensional (3-D) domains. In both cases, the governing equations, namely conservation of mass, momentum balance, energy balance, and solute transport balance, were solved using the Finite Element Method.

Measured concentration profiles and dissolution heights from the experiment samples showed that the application of a static magnetic field increased the amount of silicon transported into the melt. The magnetic field also induced a change in dissolution interface shape. This change indicates a change in flow structure in the melt. Both simulation models (axisymmetric and 3-D) predicted this change in flow structure.

In the absence of magnetic field, a flat and stable interface was observed in the experiments. In the presence of an applied field, the dissolution interface remains flat in the center but curves back into the source material near the wall. The application of the magnetic field gave rise to higher dissolution of silicon near the crucible wall. This enhanced dissolution near the wall was well predicted by the present 3-D simulation model, but not by the axisymmetric model. This indicates that this effect was due to the three-dimensionality of the melt flow.

Keywords: SiGe bulk single crystal, LPD growth method, Dissolution, Convection, Diffusion, Magnetic field, Stabilized finite element techniques.

[1] University of Limoges, SPCTS UMR CNRS 7315, European Center for Ceramics, Limoges, France.

[2] University of Annaba, LR3MI Lab., Mechanical Engineering Department, PB 12, Annaba, Algeria.

[3] University of Constantine I, Mechanical Engineering Department, Constantine, Algeria.

[4] Crystal Growth Laboratory, University of Victoria, Victoria, BC, Canada, V8W 3P6.

1 Introduction

Crystal growth is a solidification process that produces solid materials of single crystalline structure. Most bulk single crystals of semiconductors are grown from the liquid phase (melt and solution) [Müller and Ostrogorsky (1994); Dost and Lent (2007); Mechighel (2013)].

The solution growth techniques such as Liquid Phase Electroepitaxy (LPEE), Liquid Phase Diffusion (LPD), and the Traveling Heater Method (THM) and the melt growth techniques such as Bridgman, Czochralski (CZ), Vertical Gradient Freezing (VGF), and Float Zone (FZ) are used to grow single crystals of semiconductor materials that are extremely valuable in the development of electronic and optoelectronic devices [Dost and Lent (2007); Lappa (2005); Gulluoglu and Tsai (2000)]. Wafers cut from such crystals require uniform electrical properties to ensure a higher reproducibility and yield of such devices [Deal (2004)]. Consequently, there is enormous economic motivation to produce homogeneous crystals. Hence, developments in the science and technology of crystal growth are continually sought to meet increasingly precise wafer specifications required by chip manufacturers.

The literature on crystal growth processing, both experimental and/or numerical, is very rich. These studies have addressed various issues involving the application of magnetic fields, convective flow structures, flow stability, flow suppression, interface stability, and growth rates. For instance, convective flow structures, the effect of applied magnetic fields on flow structures, growth interface shapes, and growth rates in solution crystal growth techniques such as LPD may be found in [Yildiz, Dost and Lent (2005); Yildiz, Dost and Lent (2006); Yildiz, Dost and Yildiz (2006); Armour, Dost and Lent (2007); Yildiz and Dost (2007a); Yildiz and Dost (2007b); Armour, Yildiz, Yildiz and Dost (2008)], LPEE in [Armour, Sheibani, and Dost (2006); Liu, Okano, and Dost (2002)], and THM in [Okano, Nishino, Ohkubo and Dost (2002); Liu, Dost, Lent and Redden (2003); Kumar, Dost and Durst (2007)].

Although theoretical, numerical, and/or experimental investigations of morphological instability in melt/solution crystal growth over the past half-century have provided a great deal of insight into the physics of the phenomenon, accurate prediction of instabilities in semiconductors has proven, however, to be difficult. This is mainly attributable to the fact that semiconductors are facet-forming materials with highly anisotropic properties. Interfacial kinetics play a major role in the solidification of these materials, but the underlying kinetics mechanisms [Deal (2004); Sampath and Zabaras (2001); Mechighel (2013)] influencing morphological stability are still largely undiscovered. This is due in part to experimental difficulties associated with fine control of the process parameters and an inability to monitor processes occurring at the solid/liquid interface.

Recently, a series of dissolution experiments were performed in a crucible similar to that used in the LPD and Melt-Replenishment Czochralski (Cz) growth systems [Armour and Dost (2009)] (schematically shown in Fig. 1) with and without the application of a static vertical magnetic field. The measured concentration profiles from the samples processed with and without the application of magnetic field showed that the amount of silicon transport into the melt was slightly higher in the samples processed under magnetic field, and there was a substantial difference in dissolution interface shape indicating a change in flow structure in the melt. Without an applied field, a flat and stable interface was observed. In the presence of an applied field, however, the dissolution interface remained flat in the center but dramatically curved back into the source material near the crucible wall. This indicated a far higher dissolution rate at the edge of the silicon source.

In order to shed light on these experimental observations, numerical simulations using both axisymmetric and 3-D simulation domains were carried out for this dissolution process. Various levels of applied magnetic field were considered. The objectives were i) to predict the experimental observations on dissolution rates and enhanced mass transport near the wall in the melt, ii) to predict the flow patterns and concentration distributions in the melt, iii) to have a better understanding for the diffusion process in the melt which will be very beneficial in growth of SiGe single crystals from the germanium side, iv) to examine the influence of convective flow on dissolution of silicon, and v) to determine the limit of applicability of the axisymmetric model in predicting these effects.

The present simulation results showed that both the axisymmetric and 3-D models could predict the experimentally observed enhanced dissolution rates under magnetic field and also the associated changes in flow structure in the melt. The axisymmetric model was also capable of predicting the dissolution interface shape under magnetic field. However, the enhanced silicon dissolution near the crucible wall under magnetic field was only predicted by the 3-D model; showing the three-dimensionality of the flow field in the melt.

2 General Considerations and Mathematical Background

The setup used in the simulation is the arrangement where the silicon seed was floating on top of the germanium melt. In this case, the silicon seed covers the melt free surface. This arrangement is similar to the crucible stacking used in the LPD growth system for SiGe material [Yildiz, Dost and Lent (2005)]. A schematic for the material configuration used in this work is shown in Fig. 1. The growth crucible is of cylindrical shape and thus the samples are of cylindrical shapes with 24 mm diameter as clearly indicated in Fig. 1 in the model domain. Initially, the domain is equalized at 800˚C and it is then suddenly immersed into an 1100˚C isothermal

region.

In the present model, the liquid phase is taken as the Si-Ge solution domain (Ω) in the growth crucible (Fig. 1), and the solid phases represent the silicon poly-crystalline feed (Ω_S), and the ampoule-crucible wall (Ω_{Quatrz}). The liquid phase is considered as a mixture of two viscous and heat conducting incompressible Newtonian fluids, and is assumed to be a dilute binary solution (Ge-rich) of the solute (Si) and the solvent (Ge).

Furthermore, in the present model the following assumptions regarding the Si-Ge solution are considered: (i) thermo-physical properties, such as, the thermal con-

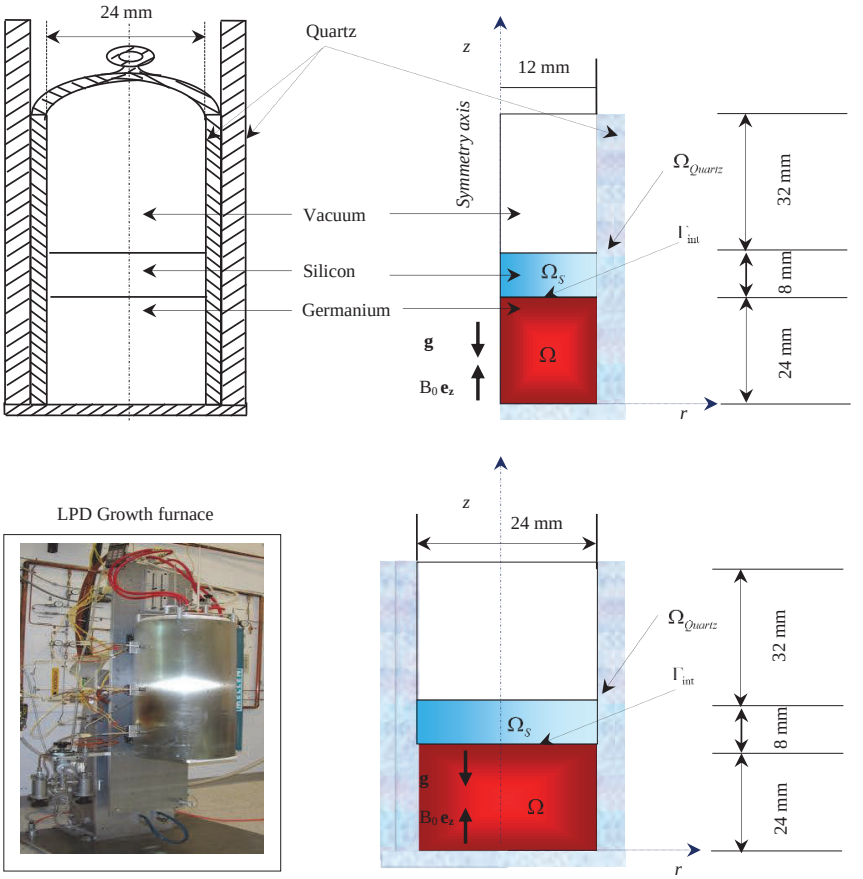

Figure 1: Schematic view of the experimental setup (upper left), the simulation axisymmetric domain (upper right), the simulation 3-D domain (lower right), and a picture of the LPD growth furnace (lower left).

ductivity k_L, the dynamic viscosity μ_L, and the thermal diffusivity $\alpha_L = k_L/\rho_L c p_L$, and the diffusion coefficient D_L of the melt are taken as constants, (ii) only laminar flow regime is considered, (iii) no viscous dissipation, and (iv) the Boussinesq approximation holds: In the Si_xGe_{1-x} liquid solution of the present setup, the density of the mixture is expressed as: $\rho_L = \rho_0 [\beta_T (T_L - T_{L,ref}) + \beta_T (C_L - C_{L,}ref)]$, where ρ_0 is the density of the reference (starting) liquid solution which is the molten germanium.

For the assumptions regarding the silicon source, thermo-physical properties, such as, the thermal conductivity k_S, and the thermal diffusivity $\alpha_S = k_S/\rho_S c p_S$ are taken as constants, moreover, no species diffusion in the silicon solid is considered ($D_S \approx 0$). Similar thermo-physical properties for the quartz solids (ampoule-crucible wall) are taken constants. The materials (silicon solid, Si-Ge solution, and quartz) thermo-physical data were compiled from [Yildiz (2005); Yildiz and Dost (2005)].

Figure 1 shows schematically the vertical cross section of the present growth system. Under the above assumptions, the three-dimensional time-dependent governing equations describing the melt (fluid) flow, heat and solute transport for the liquid phase are written in cylindrical coordinates $\mathbf{x}(r, \varphi, z)$. It is easy to write two-dimensional (axisymmetric) equations from three-dimensional equations by simply dropping the dependency on the azimuthal angle (φ) in the field dependent variables.

2.1 The Governing Equations for the liquid phase

$\Omega_t \subset \mathrm{R}^{n_{sd}}$ represents the spatial domain (Fig. 1) at time $t \in (0,\, t_{\max})$, where n_{sd} is the number of space dimensions ($n_{sd} = 2$ or 3 for respectively both the axisymmetric model and the 3-D model), Γ_t is the boundary of Ω_t. The part of the Γ_t boundary at which the velocity components, temperature, or species concentration is prescribed (essential condition) is denoted by $(\Gamma_t)_D$. The Neumann (natural) boundary conditions are imposed at the remaining part of the boundary $(\Gamma_t)_N$.

2.1.1 The Navier-Stokes Equations

Under the above assumptions, the principles of conservation of mass and balance of momentum yield the following Navier-Stokes equations, in which the velocity-pressure formulation is adopted:

$$\nabla \cdot \mathbf{u} = 0 \ \text{ on } \ \Omega_t, \ \forall t \in (0, t_{\max}) \tag{1}$$

$$\rho_L \left(\partial \mathbf{u}/\partial t\right) + \rho_L \, \mathbf{u} \cdot \nabla \mathbf{u} - \nabla \cdot \boldsymbol{\sigma} = \mathbf{F} \ \text{ on } \ \Omega_t, \ \forall t \in (0, t_{\max}) \tag{2}$$

where ρ_L, $\mathbf{u}(\mathbf{x}, t)$, with $\mathbf{x}(r, \varphi, z)$ are the mass density of the mixture (satisfying the Boussinesq approximation), mass average velocity vector, which has a radial,

an axial and an azimuthal (tangential) components denoted by (u, v and w) and the position vector (note that an axisymmetric flow field expressed in terms of the cylindrical coordinate system $\mathbf{x}(r,\varphi,z)$ where all flow variables are independent of the azimuthal angle φ). For simplicity since the velocity in the solid phases is zero, as will be shown later, in the previous equations the flow velocity in the liquid phase is designed by $\mathbf{u}(\mathbf{x},t)$ instead $\mathbf{u}_L(\mathbf{x},t)$.

In the equation (2), $\mathbf{F}(\mathbf{x},t)$ represent the external body forces (which represent here both the gravitational vector contribution (thermosolutal buoyancy force $\mathbf{F}_{buoy} = \rho_L \mathbf{g}$) and the magnetic body force $\mathbf{F}_E$ (which is illustrated latter), respectively, and σ is the stress tensor given by $\sigma(p,\mathbf{u}) = -p\mathbf{I} + 2\mu\ \varepsilon(\mathbf{u})$ with the deformation rate tensor $\varepsilon(\mathbf{u}) = \left[\nabla\mathbf{u} + (\nabla\mathbf{u})^{\mathrm{T}}\right] \Big/ 2$, p the pressure, and $\mathbf{I}$ the identity tensor.

For the flow velocity field, the homogeneous Dirichlet condition (no-slip) was assumed on the entire crucible (excluding the interface $(\Gamma_{int})_t$,which is illustrated latter), thus:

$$\mathbf{u}(\mathbf{x},t) = \mathbf{0} \ \text{ on } \ [\Gamma_t - (\Gamma_{int})_t], \ \ \forall t \in (0, t_{\max}) \tag{3}$$

As initial condition (at t = 0), since the velocity field was specified $\mathbf{u}_0(\mathbf{x}) = \mathbf{0}$ (divergence–free velocity field) over the liquid domain Ω_t thus

$$\mathbf{u}(\mathbf{x},0) = \mathbf{u}_0(\mathbf{x}) = \mathbf{0} \ \text{ on } \ \Omega_0 \tag{4}$$

2.1.2 Energy transport

The balance of energy over the liquid domain Ω_t with the boundary Γ_t leads to the following time-dependent convection-conduction equation, where neither heat generation (Joule heating) nor absorption are considered, furthermore, no heat transfer by radiation is assumed:

$$\partial T_L \big/ \partial t + \mathbf{u} \cdot \nabla T_L - \alpha_L \nabla^2 T_L = 0 \ \text{ on } \ \Omega_t \ \text{ and } \ \forall t \in (0,\ t_{\max}) \tag{5}$$

where T_L represents the temperature in the liquid phase (Ω_t).

The temperature boundary conditions on all the internal boundaries of the domain (Fig. 1) (excluding the interface $(\Gamma_{int})_t$,which is illustrated latter) are assumed as continuity, which reads:

$$\mathbf{n} \cdot (\mathbf{q}_1 - \mathbf{q}_2) = 0 \ \text{ on } \ [\Gamma_t - (\Gamma_{int})_t], \ \ \forall t \in (0, t_{\max}) \tag{6}$$

where $\mathbf{q}_i = -k_i \nabla T_i$ (where, i refers to material 1 and material 2, i.e. solution/quartz).

The condition $T_{ini} = 800^{\circ}C$ was specified as the initial condition, which reads:

$$T_L(\mathbf{x},0) = T_0(\mathbf{x}) = T_{ini} \ \text{ on } \ \Omega_0 \tag{7}$$

2.1.3 Solute transport

Since there is no mass transport through the crucible wall (impermeable), and by assuming no solute (silicon) diffusion in the solid ($D_s << D_L$), the solute transport may then be given by the following time-dependent mass transport equation:

$$\partial C_L / \partial t + \mathbf{u} \cdot \nabla C_L - D_L \nabla^2 C_L = 0 \text{ on } \Omega_t \text{ and } \forall t \in (0, t_{\max}) \tag{8}$$

where C_L and D_L are the concentration and the coefficient of the diffusion of the liquid solute in the liquid phase (Si-Ge melt), respectively.

Since it was assumed that the crucible boundaries are not permeable for species transport, thus, the solutal boundary conditions (excluding the interface $(\Gamma_{int})_t$, which is illustrated latter) associated with Eq. (8) are:

$$\mathbf{n} \cdot D_L \nabla C_L = h_C = 0 \text{ on } [\Gamma_t - (\Gamma_{int})_t] \text{ and } \forall t \in (0, t_{\max}) \tag{9}$$

where h_C represents a specified species flux (Neumann condition). Furthermore, the following condition is specified as the initial condition:

$$C_L(\mathbf{x}, 0) = C_0(\mathbf{x}) = 0 \text{ on } \Omega_0 \tag{10}$$

2.1.4 Electric charge balance equation and the magnetic body force

The crucible is subjected to an applied axial static magnetic field $\mathbf{B} = B_0 \mathbf{e}_z$ with the uniform field intensity of B_0 as shown in Fig. 1. For metallic liquids, the magnetic body force $\mathbf{F}_E$ acting on the points of the liquid (domain Ω_t) may be taken simply as

$$\mathbf{F}_E = \mathbf{J} \times \mathbf{B}$$

where the contribution of electric charge is neglected, and the current density $\mathbf{J}$ is given by the Ohm's law by

$$\mathbf{J} = \sigma_e (-\nabla \phi + \mathbf{u} \times \mathbf{B}) \tag{11}$$

The current density $\mathbf{J}$ is governed by the conservation of current

$$\nabla \cdot \mathbf{J} = 0 \tag{12}$$

with the assumption that the induced fields due to the applied magnetic field are negligible [Mechighel (2013)]. This is a good approximation for metallic liquids since the magnetic Reynolds numbers are sufficiently small [Giessler, Sievert, Krieger, Halbedel, Huelsenberg, Luedke and Thess (2005); Kakimoto and Liu (2006)]. In the above equations ϕ is the electric potential and σ_e the electric

conductivity of the liquid phase. In this case the magnetic body force becomes $\mathbf{F}_E = \sigma_e\left(-\nabla\phi + \mathbf{u}\times\mathbf{B}\right)\times\mathbf{B}$.

Combining (11) and (12) leads to the following Poisson's equation

$$\nabla^2\phi = \nabla\cdot(\mathbf{u}\times\mathbf{B}) = B_0\,\mathbf{e}_z\cdot(\nabla\times\mathbf{u}) \;\text{ on }\; \Omega_t,\;\; \forall t\in(0,\,t_{\max}) \tag{13}$$

that governs the electric potential distribution.

Note that for the axisymmetric model case, since the vorticity vector, $\nabla\times\mathbf{u} = \left(\partial u/\partial z - \partial v/\partial r\right)\mathbf{e}_\varphi = \mathbf{0}$, thus the electrical potential conservation equation reduces to $\nabla^2\phi = 0$, this simplifies significantly the axisymmetric problem and hence, the resolution for this equation is not required as there was no contribution of gradient of ϕ in the magnetic body force (i.e. $\mathbf{F}_E = \sigma_e\left(\mathbf{u}\times\mathbf{B}\right)\times\mathbf{B}$).

2.2 Solid phases

The problem can be greatly simplified when assuming that there is no species diffusion in the solid, so that $\mathbf{u}_s = \mathbf{0}$ (where $\mathbf{u}_s$ is the velocity vector in the solid phases). The only governing equation needed is the energy balance:

$$\partial T_s/\partial t = \left(k_s/\rho_s cp_s\right)\nabla^2 T_s,\;\text{ on }\;\Omega_{solid},\;\;\forall t\in(0,\,t_{\max}) \tag{14}$$

where ρ_s, cp_s, and k_s are the density, specific heat and thermal conductivity of the solid phases (Fig. 1), respectively. Recall that the solid phases in the model are the polycrystalline Si source; and the quartz crucible-ampoule which are modeled as a rigid, heat conducting solid, as shown in Fig.1.

In the silicon solid phase, Ω_{solid} represents Ω_S, (Fig. 1), and the temperature is denoted by T_S, the conditions on Γ_{int} (illustrated later), continuity conditions on silicon source/crucible boundary and top silicon/vacuum boundary together provide the required boundary conditions for resolution of the heat transport problem. (The vacuum above the surface is assumed to be a gas of negligible viscosity and conductivity).

For the quartz crucible, Ω_{solid} represents Ω_{Quartz}, (Fig. 1), and the temperature is denoted by T_{Quartz}, the thermal boundary conditions for the outer vertical wall, and bottom surface of the quartz crucible are expressed as a specified temperature (1100°C). At the top surface of the domain the flux was set to zero. Furthermore, perfect thermal contacts and continuous heat flux at the silicon seed/crucible, solution/crucible and inner crucible boundaries were assumed.

2.3 Conditions at silicon source/melt (dissolution) interface

The interfacial system of the present study consists of two non-reacting components, Ge and Si, and two phases; the liquid phase (L) (Si-Ge melt assumed as a

dilute binary liquid mixture (Ge-rich) of the solute (Si) and the solvent (Ge)) and the solid phase (S) (silicon source).

The solid/liquid (source/melt or dissolution) interface is a complicated boundary where the imposed conditions must account for interfacial transport of energy and mass. Indeed, the dissolution interface is not only a source and sink for thermal energy and components, but it moves as phase change takes place. The conditions required to establish such an interface can be determined using thermodynamics, (i.e. assuming the interface is an equilibrium state of the system). Furthermore, the driving force for phase transformation (i.e. dissolution in the present study) can be described by a deviation from this equilibrium state [Mechighel (2013)].

General boundary conditions at a solid/liquid interface may be written as:

$$T_S = T_L = T_m^0 + m_L C_L - 2\gamma_{SL}\Upsilon/\Delta S^0 \tag{15a}$$

$$k_S\left(\nabla T_S \cdot \mathbf{n}\right) - k_L\left(\nabla T_L \cdot \mathbf{n}\right) = -L_{fV}\left(\mathbf{u}^{int} - \mathbf{u}\right)\cdot \mathbf{n} \tag{15b}$$

$$D_L\left(\nabla C_L \cdot \mathbf{n}\right) = C_L\left(\kappa - 1\right)\left(\mathbf{u}^{int} - \mathbf{u}\right)\cdot \mathbf{n} \tag{15c}$$

where T_m^0 is the melting temperature of pure Ge, m_L is the liquidus slope given by the two-component phase diagram, Υ is the local mean curvature of the interface (positive for convex surfaces viewed from the liquid), ΔS^0 is the entropy of fusion per unit volume for pure (Ge), γ_{SL} is the interfacial energy per unit area between the solid and liquid phases, $\mathbf{n}$ is the unit normal vector to a point solid/liquid interface pointing toward the liquid; $\mathbf{u}^{int}$ is the velocity of the solid/liquid interface in the reference (fixed) frame at that point, and $L_{fV} < 0$ is the latent heat of fusion (enthalpy of fusion) for the solid (Si source) per unit volume, assumed identical for the solute and $\kappa = C_S/C_L$ is the equilibrium distribution coefficient of the solute.Here all quantities are associated with the solid/liquid (S/L) interface boundary.

Assumptions at the dissolution interface

-The inclusion of the liquid velocity $\mathbf{u}$ at the dissolution interface in previous equations is necessary if the density of the solid and liquid are not equal [Deal (2004)]. The resulting shrinkage or expansion upon dissolution will alter the velocity of the interface and affect the transport of components and heat, and $\mathbf{u}$ accounts for this. However, since the experimentally observed dissolution rate of silicon source into the solution is very small, so the velocity components (u, v and w) of fluid particles at the dissolution interface can be neglected in the present system (thus $\mathbf{u}\cdot\mathbf{n} = 0$) [Armour and Dost (2009)].

-As mentioned earlier, assuming the interface is at an equilibrium state of the system, means that the local thermodynamic equilibrium ($T_S = T_L = T_{eq}$) is reached at the interface, the solute concentration at the dissolution interface is determined

from the Si-Ge binary phase diagram, namely $C_{eq} = fn(T_{eq})$, which is written for the liquid (C_L^{eq}) and solid (C_S^{eq}) equilibrium compositions for the Ge-rich side of the phase diagram. On the dissolution interface we adopt the following saturation concentration (in molar concentration of silicon) predicted from the Si-Ge phase diagram:

$$C_L^{eq} = C_L^{dis} = 2005.62 \times \left[(cc_L \times 28.086)/((72.64 \times (1.0 - cc_L) + 28.086 \times cc_L))\right]$$

and

$$C_S^{eq} = C_S^{dis} = 2005.62 \times \left[(cc_S \times 28.086)/((72.64 \times (1.0 - cc_S) + 28.086 \times cc_S))\right]$$

where

$cc_L = \left[4 \times 10^{-6} \times (T_{eq} - 273.15)^2 - 0.007 \times (T_{eq} - 273.15) + 3.361\right]$ and

$$cc_S = \left\{ \begin{array}{l} 6 \times 10^{-9} \times (T_{eq} - 273.15)^3 - 1 \times 10^{-5} \times (T_{eq} - 273.15)^2 \\ +0.0198 \times (T_{eq} - 273.15) + 7.044 \end{array} \right\}$$

-Furthermore, we assume that at the dissolution interface the contribution of latent heat is neglected since the dissolution interface velocity is very small. Thus, the energy balance at the interface, Eq. (15b), reduces to: $k_S(\nabla T_S \cdot \mathbf{n}) - k_L(\nabla T_L \cdot \mathbf{n})$=0.

-We then write the mass balance equation at the dissolution interface, i.e. Eq. (15c), $D_L(\nabla C_L \cdot \mathbf{n}) = C_L(\kappa - 1)\left(\mathbf{u}^{int}\right) \cdot \mathbf{n}$. However, since the interface velocity is small we take $\mathbf{u}^{int} = \mathbf{0}$, and thus the mass balance at the interface is excluded. Then, the conditions at the dissolution interface $(\Gamma_{int})_t$ become

$$C_L = C_L^{dis} = C_L^{eq} \text{ at } T_{dis}, \ (u = 0, \ v = 0 \text{ and } w = 0), \text{ and } k_L \frac{\partial T_L}{\partial \mathbf{n}} = k_S \frac{\partial T_S}{\partial \mathbf{n}} \quad (16)$$

where C_L^{dis} and T_{dis} are respectively the equilibrium mass fractions of the solute and the temperature at the dissolution interface ($T_{dis} = T_{eq} = T_S = T_L$).

2.4 Symmetry conditions (used only for the axisymmetric model):

At the axis of symmetry, we use symmetry conditions. Also for physical (finite) results, it is required that the radial velocity component be zero [Yildiz and Dost (2005)]. Thus,

$$u = 0 \text{ and } \partial v/\partial r = 0 \text{ on the symmetry axis } (r = 0), \ \forall t \in (0, t_{\max}) \quad (17a)$$

$$\mathbf{n} \cdot \alpha_L \nabla T = h_T = 0 \text{ on the symmetry axis } (r = 0), \ \forall t \in (0, t_{\max}) \quad (17b)$$

$$\mathbf{n} \cdot D_L \nabla C = h_C = 0 \text{ on the symmetry axis } (r = 0), \ \forall t \in (0, t_{\max}) \quad (17c)$$

3 Numerical resolution

3.1 The ST-GLS formulation for unsteady incompressible fluid flow

Since the dissolution interface velocity is assumed to be negligible in the present study so the space-time Galerkin/least-square (ST-GLS) finite element formulation for incompressible fluid flows is used here. This formulation is used in order to prevent numerical instabilities encountered when using the standard Galerkin finite element method (details on this technique can be found in works by Tezduyar and Coworkers [Tezduyar (1992); Tezduyar, Mittal, Ray and Shih (1992)]. In the present work, this stabilized finite element formulation was utilized using *equal-order* interpolation velocity-pressure elements as proposed by [Tezduyar, Mittal, Ray and Shih (1992)].

Firstly, the formulation assumes that the spatial domain is fixed in time; this implies that the subscript t is dropped from the symbols Ω_t and Γ_t [Tezduyar (1992)]. In the space-time finite element formulation, the time interval $(0,\, t_{\max})$ is partitioned into subintervals $I_n = (t_n,\, t_{n+1})$, where t_n and t_{n+1} belong to an ordered series of time levels $0 = t_0 < t_1 < \cdots < t_N = t_{\max}$. The space-time slab Q_n is defined as the space-time domain $\Omega \times I_n$. The lateral surface of Q_n is denoted by P_n; this is the surface described by the boundary Γ, as t traverses I_n. Similarly, P_n is decomposed into $(P_n)_D$ and $(P_n)_N$ with respect to the type of boundary condition being imposed (as shown in Eq. 3, since we have only the Dirichlet part, including the dissolution interface (Eq. 16), thus $P_n = (P_n)_D \cup (P_n)_N = (P_n)_D$).

Finite element discretization of a space-time slab Q_n is achieved by dividing it into elements Q_n^e, $e = 1, 2, \cdots, (n_{el})_n$, where $(n_{el})_n$ is the number of elements in the space-time slab Q_n. Associated with this discretization, by adopting the standard notation of [Tezduyar (1992); Tezduyar, Mittal, Ray and Shih (1992)]) we define the following finite element interpolation and variational function spaces for velocity and pressure:

$$\left(\mathbf{S}_{\mathbf{u}}^h\right)_n = \left\{ \mathbf{u}^h \,\middle|\, \mathbf{u}^h \in \mathbf{H}_0^{1h}(Q_n)\,,\ \mathbf{u}^h = \mathbf{0} \ \text{ on } \ (P_n)_D \text{-} (P_n)_{int} \text{ and } \mathbf{u}^h \cdot \mathbf{n} = 0 \ \text{ on } \ (P_n)_{int} \right\}$$

$$\left(\mathbf{V}_{\mathbf{u}}^h\right)_n = \left\{ \mathbf{w}^h \,\middle|\, \mathbf{w}^h \in \mathbf{H}_0^{1h}(Q_n)\,,\ \ \mathbf{w}^h = \mathbf{0} \ \ (P_n)_D \text{-} (P_n)_{int} \text{ and } \mathbf{w}^h \cdot \mathbf{n} = 0 \ \ \text{on } \ (P_n)_{int} \right\}$$

$$\left(S_p^h\right)_n = \left(V_p^h\right)_n = \left\{ \left. q^h \,\right|\, q^h \in L^{2h}(Q_n) \Big/ \mathbb{R} \right\}$$

The *GLS* technique is defined by imposing that the stabilization term added is an *element-by-element* weighted least-squares formulation of the original Eq. 2 to assure the numerical stability of the computations (see [Tezduyar (1992); Tezduyar, Mittal, Ray and Shih (1992)] for further details). Using the standard notation of

[Tezduyar (1992); Tezduyar, Mittal, Ray and Shih (1992)], the space-time formulation of Eqs. 1, 2, 3 and 4 can be written as follows:

Start with $\left(\mathbf{u}^h\right)_0^- = (\mathbf{u}_0)^h$, sequentially for Q_1, Q_2, ..., Q_{n-1}, given $\left(\mathbf{u}^h\right)_n^-$, find $\mathbf{u}^h \subset \left(\mathbf{S}_{\mathbf{u}}^h\right)_n$ and $p^h \subset \left(S_p^h\right)_n$, such that: $\forall \mathbf{w}^h \subset \left(\mathbf{V}_{\mathbf{u}}^h\right)_n$ and $\forall q^h \subset \left(V_p^h\right)_n$, we have:

$$\begin{aligned}
&\int_{Q_n} \mathbf{w}^h \cdot \rho\left(\frac{\partial \mathbf{u}^h}{\partial t} + \mathbf{u}^h \cdot \nabla \mathbf{u}^h\right) dQ + \int_{Q_n} \varepsilon\left(\mathbf{w}^h\right) : \sigma\left(p^h, \mathbf{u}^h\right) dQ - \int_{(P_n)_N} \mathbf{w}^h \cdot \mathbf{h}_N \, dP \\
&+ \int_{Q_n} q^h \nabla \cdot \mathbf{u}^h \, dQ - \int_{Q_n} \mathbf{w}^h \cdot \mathbf{F} \, dQ + \int_{\Omega} \left(\mathbf{w}^h\right)_n^+ \cdot \left\{\left(\mathbf{u}^h\right)_n^+ - \left(\mathbf{u}^h\right)_n^-\right\} d\Omega \\
&+ \sum_{e=1}^{(n_{el})_n} \int_{Q_n^e} \tau_{stab}^{GLS} \left[\rho\left(\frac{\partial \mathbf{w}^h}{\partial t} + \mathbf{u}^h \cdot \nabla \mathbf{w}^h\right) - \nabla \cdot \sigma\left(q^h, \mathbf{w}^h\right) \quad - \mathbf{F}\right] \cdot \\
&\cdot \left[\rho\left(\frac{\partial \mathbf{u}^h}{\partial t} + \mathbf{u}^h \cdot \nabla \mathbf{u}^h\right) - \nabla \cdot \sigma\left(p^h, \mathbf{u}^h\right) \quad - \mathbf{F}\right] dQ = 0
\end{aligned} \tag{18}$$

Note that the term $\int_{(P_n)_N} \mathbf{w}^h \cdot \mathbf{h}_N \, dP = \int_{(P_n)_N} \mathbf{w}^h \cdot (\sigma \cdot \mathbf{n}) \, dP = 0$ (since in our case $(P_n)_N = \varnothing$). The coefficient τ_{stab}^{GLS} determines the weight of such added terms, and in this weak form, following the notation used in [Tezduyar (1992)], we write $\left(\mathbf{u}^h\right)_n^{\pm} = \lim_{\delta \to 0} \mathbf{u}^h(t_n \pm \delta)$, $\int_{Q_n} (\cdots) \, dQ = \int_{I_n} \int_{\Omega} (\cdots) \, d\Omega \, dt$ and $\int_{P_n} (\cdots) \, dP = \int_{I_n} \int_{\Gamma} (\cdots) \, d\Gamma \, dt$.

For various ways of calculating matrix τ_{stab}^{GLS}, see for instance [Tezduyar (1992); Shakib (1988); Hauke and Hughes (1998); Polner (2005); Förster (2007)]. In the present study, this was implemented in COMSOL package (see [COMSOL Multiphysics Modeling Guide (2008)]).

The finite element interpolation functions are discontinuous in time. The fully discrete equations can be solved one space-time slab at a time (a fractional-step procedure). The memory needed for the global matrices involved in this method is quite extensive. Iteration methods can be employed to substantially reduce the cost involved in solving the linear equation systems arising from the space-time finite element discretization. Here, resolution was achieved using the generalized minimal residual (GMRES) method [Saad and Schultz (1986); COMSOL Multiphysics Modeling Guide (2008)].

3.2 Streamline Upwind Petrov-Galerkin (SUPG) formulation for the heat transport

For the heat transport equation, we adopt the SUPG stabilization given by [Ed Akin and Tezduyar (2004)]. Consider the initial boundary value problem given by the unsteady convection-conduction equation, Eq. 5, and its associated boundary and initial conditions, Eqs. 6 and 7. The principle of the SUPG stabilization technique is defined by taking a perturbation as the following: $\mathscr{P}(w) = \mathbf{u} \cdot \nabla w$. This will

be introduced in the weak form of the problem, with being the weighting function. Thus

$$\begin{aligned}&\int_{\Omega} w\left(\frac{\partial T_L}{\partial t}+\mathbf{u}\cdot\nabla T_L\right)d\Omega+\int_{\Omega}\nabla w\cdot(\alpha_L\nabla T_L)\,d\Omega\\&-\int_{\Gamma_N} w\,h_T\,d\Gamma+\sum_{e=1}^{n_{el}}\int_{\Omega^e}\tau^T_{SUPG}\left(\mathscr{P}(w)\mathscr{R}(w)\right)d\Omega=0\end{aligned}\tag{19}$$

where $\mathscr{R}(w)$ is the residual of the equation of energy, Eq. 5.

Using a suitably-defined finite-dimensional trial solution and interpolation function spaces (further details, see [Ed Akin and Tezduyar (2004)]), the stabilized SUPG finite element formulation of the previously written energy equation with boundary and initial conditions can be written as follows.

Find $T_L^h \in S_T^h$ such that $\forall w^h \in V_T^h$

$$\begin{aligned}&\int_{\Omega} w^h\left(\frac{\partial T_L^h}{\partial t}+\mathbf{u}^h\cdot\nabla T_L^h\right)d\Omega+\int_{\Omega}\nabla w^h\cdot\left(\alpha_L\nabla T_L^h\right)d\Omega-\int_{\Gamma_N} w^h\,h_T\,d\Gamma\\&+\sum_{e=1}^{n_{el}}\int_{\Omega^e}\tau^T_{SUPG}\left(\left(\mathbf{u}^h\cdot\nabla w^h\right)\left(\frac{\partial T_L^h}{\partial t}+\mathbf{u}^h\cdot\nabla T_L^h-\alpha_L\nabla^2 T_L^h\right)\right)d\Omega=0\end{aligned}\tag{20}$$

Here n_{el} is the number of elements and Ω^e is the element domain corresponding to element e. τ^T_{SUPG} is the SUPG stabilization parameter. For various ways of calculating τ^T_{SUPG}, see for instance [Tezduyar and Osawa (2000); Ed Akin and Tezduyar (2004)]. In the present study, this was implemented in COMSOL package.

Finally, the finite element discretization of this weak form yields a system of semi-discrete equations for $t \in (0, t_{\max})$. In order to trace the transient response, this system of semi-discrete equations can be advanced in time by suitable finite difference schemes such as the θ family methods. A fully implicit method known as "Backward Differentiation Formulas" (BDF) is used [Donea and Huerta (2003); COMSOL Multiphysics Modeling Guide (2008)].

3.3 SUPG FEM for solute transport equation

The same SUPG stabilization technique is used for the solute transport equation. Using a suitably-defined finite-dimensional trial solution and interpolation function spaces, the stabilized finite element formulation of the previously written species equation (Eq. 8) with boundary and initial conditions (Eqs. 9 and 10) can be written as follows:

Find $C^h \in S_C^h$ such that $\forall w^h \in V_C^h$:

$$\begin{aligned}&\int_{\Omega} w^h\left(\frac{\partial C_L^h}{\partial t}+\mathbf{u}^h\cdot\nabla C_L^h\right)d\Omega+\int_{\Omega}\nabla w^h\cdot\left(D_L\nabla C_L^h\right)d\Omega-\int_{\Gamma_N} w^h h_C\,d\Gamma\\&+\sum_{e=1}^{n_{el}}\int_{\Omega^e}\tau^C_{SUPG}\left(\left(\mathbf{u}^h\cdot\nabla w^h\right)\left(\frac{\partial C_L^h}{\partial t}+\left(\mathbf{u}^h\cdot\nabla C_L^h\right)-D_L\nabla^2 C_L^h\right)\right)d\Omega=0\end{aligned}\tag{21}$$

Here τ_{SUPG}^{C} is the SUPG stabilization parameter (for solute transport equation). For various ways of calculating τ_{SUPG}^{C}, see for instance [Franca; Frey and Hughes (1992); Tezduyar and Osawa (2000)]. In the present study, this was implemented in COMSOL package.

3.4 Heat transport by conduction in the solid phases

The classical Standard Galerkin formulation [Donea and Huerta (2003); COMSOL package] is used for Eq. 14, with the corresponding boundary and initial conditions. Further details about the mathematical modeling and solution methodology are illustrated in the article by [Mechighel, Armour, Dost and Kadja, (2011)].

4 Results and discussion

The 3-D simulation conducted in the absence of magnetic field exhibited a decaying dissolution phenomenon, and showed an expected diffusion-dominated behavior in the region close to the dissolution interface, in agreement with the experimental observation of [Armour and Dost (2009)] (Fig. 2). Transport into the Ge-rich melt is relatively slow and continues to slow down as the concentration gradient flattens. Mathematically, this means that in Eq. 8 the diffusive term, $(-\nabla \cdot (D_L \nabla C_L) = -D_L \nabla^2 C_L)$, is dominant compared with the convective term, $(\mathbf{u} \cdot \nabla C_L)$, in this region. In fact, this is due to the physics of the experimental configuration. In this system, the silicon source placed at the top of the melt dissolves, under the applied temperature profile, into the Ge-rich melt, and then diffuses downward in the opposite direction to the gravity-induced buoyancy force. Due to the large density difference between the Si solute and the Ge-rich melt, the lighter silicon solute is buoyant, and the diffusion of silicon acts to stabilize the melt against natural (thermosolutal) convection. This makes the silicon transport in this system diffusion dominated, and naturally leads to slower dissolution rates. At the center of the melt and near the crucible wall, however, convective flow is present as illustrated in the following manner.

The nature of the flow in the melt can be quantified by determining the relative contributions of convection and diffusion by calculating the ratio of the buoyancy force to the viscous force, known as the thermal Grashof number, $Gr_T = g\beta_T (G_T) R^4 / \upsilon_L^2$. For Gr_T values less than 10^4, viscosity dominates and convection is minimal (Stokes flow). However, if Gr_T is greater than 10^4, convection is present, and the diffusion boundary layer is truncated by the melt flow. Taking a lower limit for the present study (with the melt radius R of 12 mm and a temperature gradient G_T of 5 K/cm) we calculate $Gr_T \approx 6 \times 10^5$. This means that a relatively weak convective flow (thermal convection) was present in the melt. In addition, an upper bound for the size of the diffusion boundary layer is estimated by (D_L / R_{dis}),

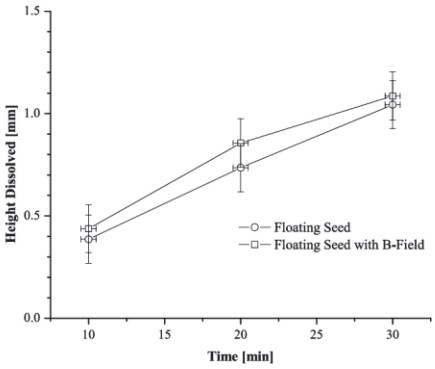

(a) experiment [Armour and Dost (2009)]

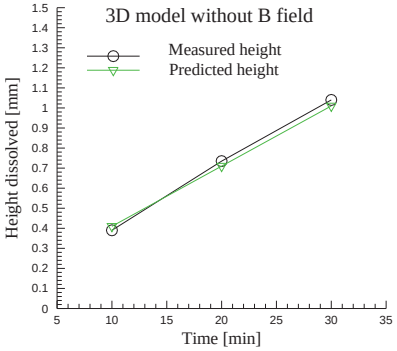

(b) 3-D simulation

Figure 2: Average height of silicon dissolved into Ge-rich melt: (a) experiment conducted with no field and under a 0.8 Tesla magnetic field level [Armour and Dost (2009)]; (b) comparison between the numerically predicted and measured dissolution heights. Prediction is in good agreement with experiment. Indeed, the maximum relative error between the simulation and experimental results is less than 6%.

using the smallest dissolution rate. For $R_{dis} = 2.5$ mm/hr, this is 36 mm. Therefore, since convection was present, the diffusion boundary layer in the system was less than 36 mm.

To provide further insight into the nature of the melt flow and mixing in the present crucible configuration, numerical simulations using both axisymmetric and 3-D models were carried out without and with the application of magnetic field. The numerically predicted concentration and melt flow velocity fields are presented in Figs. 3, 4, 5. The components of melt flow velocity (u, v and w) are also graphically shown in Figs. 6, 7, 8.

Computed flow patterns in the melt after 20 minutes of dissolution are graphically represented by flow velocity vectors in Fig. 3. The rotation of the thermosolutal convection cell is counterclockwise (Fig. 3a). In 3-D simulation, this is an annular roll (Fig. 3b and 3d). Near the crucible wall (i.e. sides of the sample) fluid moves up toward the dissolution interface, and then it travels along the dissolution interface toward the center, finally turning downwards in the direction of the crucible bottom surface. Along the dissolution interface near the center of the sample, flow is very weak, and consequently, the solute transport is diffusion dominated in this region. Slow dissolution (lower dissolution rate) in this region results in a semi-mixed melt.

However, a stronger flow along the vertical wall (sides) of the domain leads to a better mixing in the melt and gives rise to relatively faster dissolution rates of the source at the edge. Indeed, the concentration profile around the dissolution interface shows that silicon is being mixed away from the region near the crucible wall towards the center of the melt (Fig. 3b and 3c).

The stable flow structure (caused by silicon buoyancy in the melt) results in a flat dissolution interface. The most significant difference with the application of the magnetic field is the shape of the dissolution interface as seen in Fig. 9 (taken from reference [Armour and Dost 2009]). In Fig. 9, we see the photos of the

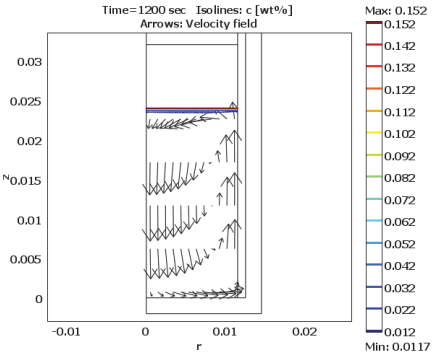

(a) axisymmetric model

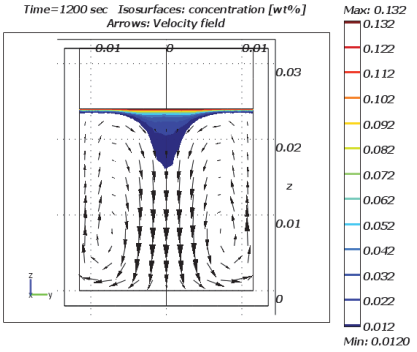

(b) 3-D model (vertical cross section)

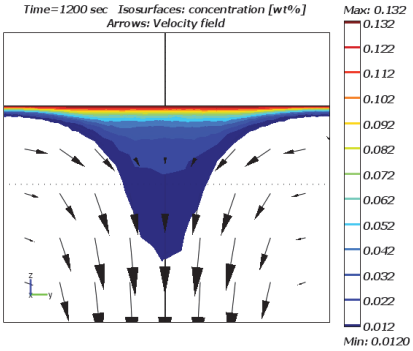

(c) 3-D model: concentration field in the region near the center of the interface

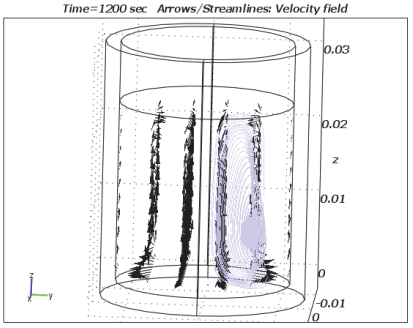

(d) 3-D model: streamlines

Figure 3: Results after 20 min of dissolution with no magnetic field. Arrows indicate the flow structure, and isolines/isosurfaces illustrate the solute concentration distribution. In the 3-D simulation the dissolution pattern clearly indicates that it is more concentrated in the center.

polished surfaces of the cross-sections of two processed samples, which are obtained by cutting through the center of the cylindrical processed samples at the end of the dissolution experiment. In this figure, the photo of the cross-section of the processed sample on the right (under magnetic field) clearly shows the enhanced dissolution (more silicon dissolution) near the crucible wall compared with that in the photo on the left (with no magnetic field). On the left, we see that the silicon dissolution interface remains almost flat, but on the right, more silicon dissolved near the wall leading to a curved interface that is visible in the photo.

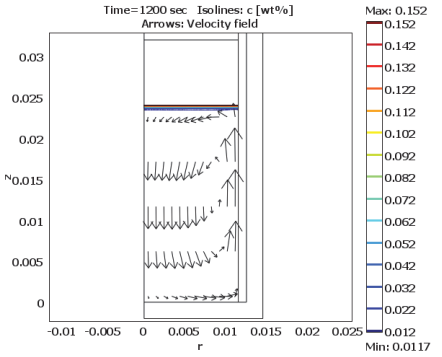

(a) axisymmetric model

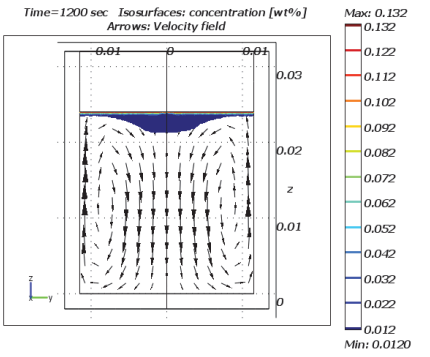

(b) 3-D model (vertical cross section)

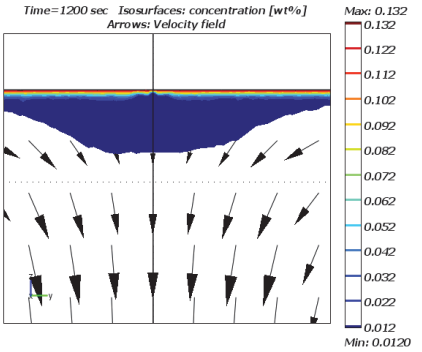

(c) 3-D model: concentration field in the region near the center of the interface

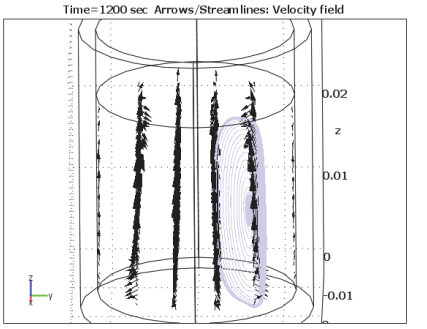

(d) 3-D model: streamlines

Figure 4: Results after 20 min of dissolution under a 0.2 Tesla field. Arrows indicate the flow structure and isolines/isosurfaces illustrate the solute concentration distribution. In the 3-D simulation the dissolution pattern clearly indicates that it is more concentrated in the center (but is less pronounced than the simulation with no applied field).

As mentioned earlier, the change observed in the interface shape indicates the effect of the applied magnetic field on the melt flow. This expected change in the melt flow is well predicted by the present 3-D numerical simulation (as shown in Figs. 3 and 5). The rotation of the thermosolutal convection roll is *clockwise* under magnetic field (Figs. 5b and 5d). One may explain the numerically predicted flow and dissolution patterns as follows. The downward strong warm flow, due to the combined effect of gravitational and magnetic body forces, is observed in the regions near to the crucible wall (Fig. 5b and 5d), due to solute rejection in the melt. The flow starts from the region near the interface edge (i.e. edge of the silicon source)

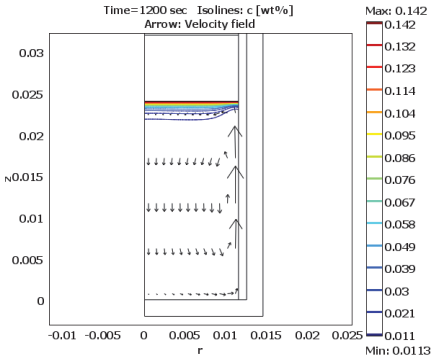

(a) axisymmetric model

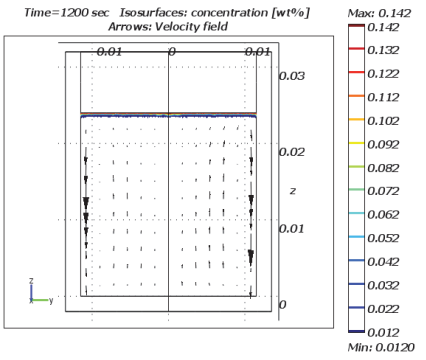

(b) 3-D model (vertical cross section)

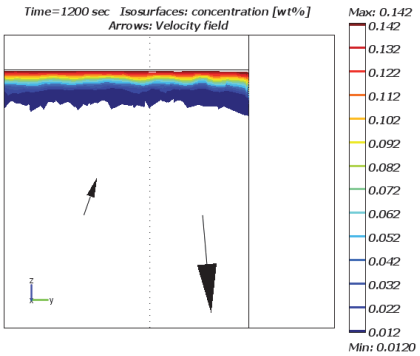

(c) 3-D model: concentration field in the region near the edge of the interface

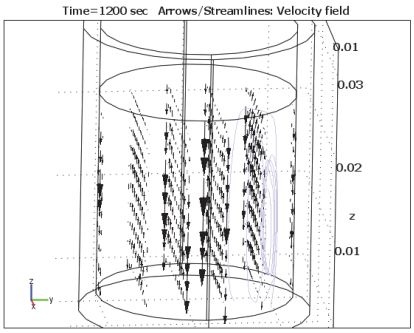

(d) 3-D model: streamlines

Figure 5: Results after 20 min dissolution with a 0.8 Tesla applied field. Arrows indicate the flow structure and isolines/isosurfaces illustrate the concentration profile. In the 3-D simulation the dissolution pattern indicates that it is more concentrated near the edge.

and moves towards the crucible bottom surface, supplying and enriching the melt with the dissolved solute. The solute transport by convection in this region leads to further dissolution from the source (faster dissolution at the edge of the silicon

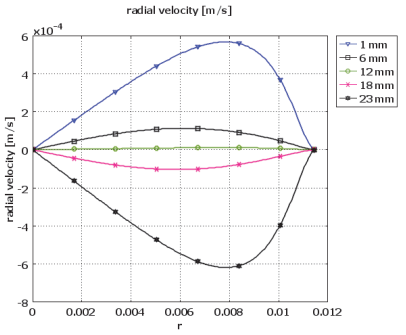

(a) axisymmetric model: radial velocity plotted at different radial positions

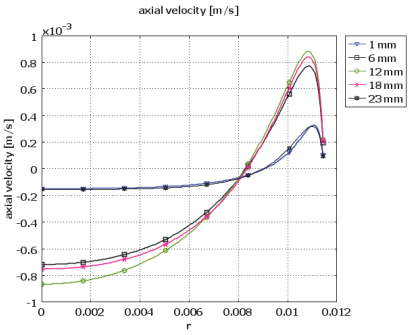

(b) axisymmetric model: axial velocity plotted at different radial positions

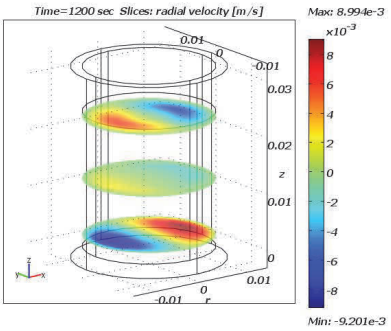

(c) 3-D model: radial velocity

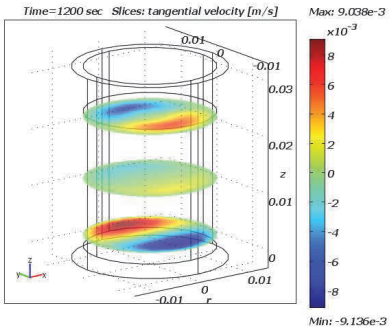

(d) 3-D model: tangential velocity

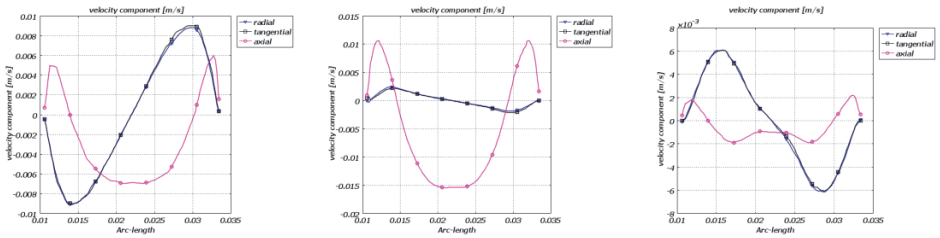

z = 2 mm z = 12 mm z = 23 mm

(e) 3-D model: radial, axial and tangential components of velocity at different radial positions

Figure 6: Results after 20 min of dissolution with no applied field. Slices indicate the radial and tangential velocity components plotted at different radial positions (z = 2 mm, 12 mm and 23 mm).

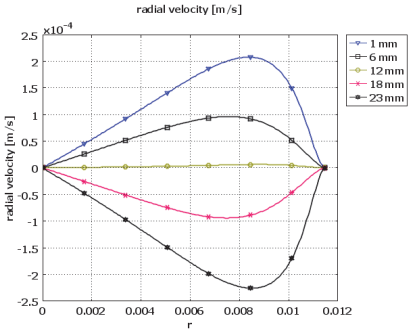

(a) axisymmetric model: radial velocity plotted at different radial positions

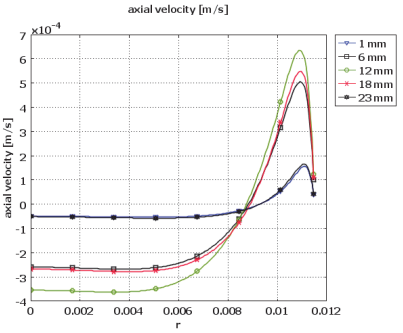

(b) axisymmetric model: axial velocity plotted at different radial positions

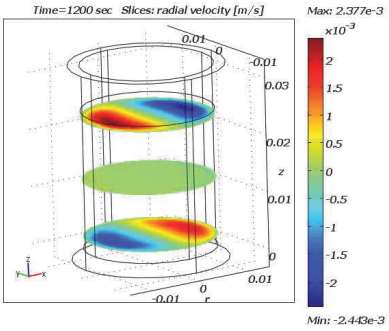

(c) 3-D model: radial velocity

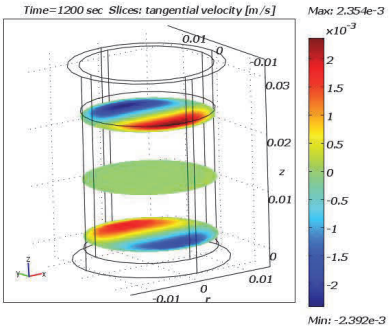

(d) 3-D model: tangential velocity

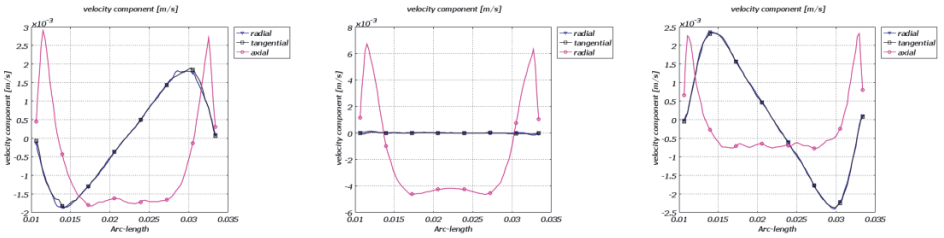

z = 2 mm z = 12 mm z = 23 mm

(e) 3-D model: radial, axial and tangential components of velocity at different radial positions

Figure 7: Results after 20 min of dissolution with 0.2 Tesla applied field. Slices indicate the radial and tangential velocity components plotted at different radial positions (z = 2 mm, 12 mm and 23 mm).

source). Near the crucible bottom surface, a warmer downward flow turns towards the center of the melt and brings the dissolved solute to the center (Fig. 5b and 5d) which results in well-mixed regions along the sides and the center of the melt.

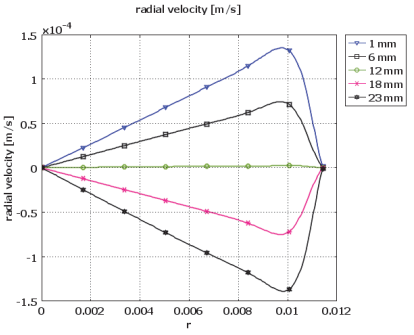

(a) axisymmetric model: radial velocity plotted at different radial positions

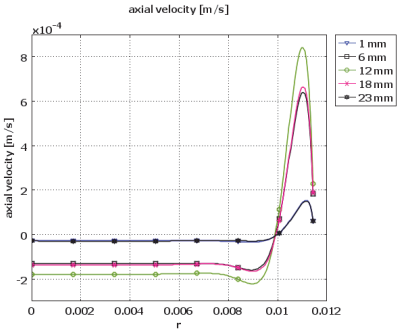

(b) axisymmetric model: axial velocity plotted at different radial positions

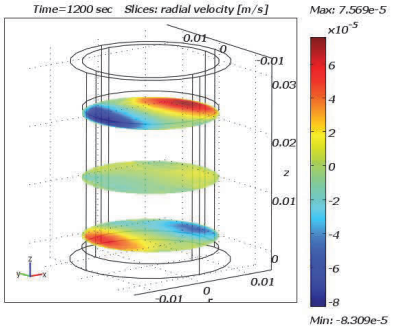

(c) 3-D model: radial velocity

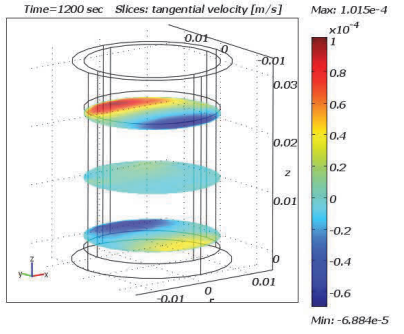

(d) 3-D model: tangential velocity

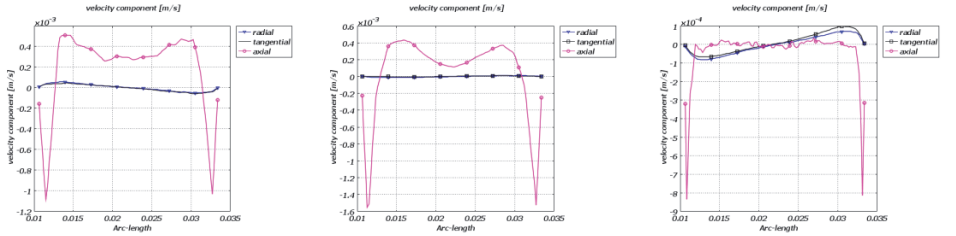

z = 2 mm z = 12 mm z = 23 mm

(e) 3-D model: radial, axial and tangential components of velocity at different radial positions

Figure 8: Results after 20 min of dissolution with 0.8 Tesla applied field. Slices indicate the radial and tangential velocity components plotted at different radial positions (z = 2 mm, 12 mm and 23 mm).

The observed stronger downward flow (driven by the gravitational body force) at the center was reversed in direction with the applied magnetic field (Fig. 3b and 5b). In the region close to the center of the interface, the melt flow is almost absent and the solute transport is diffusion-dominated. This naturally leads to far slower dissolution rates at the center and results in semi-mixed region at the center of the melt near the dissolution interface. It is important to note that the axisymmetric model does not predict these trends (Fig. 3a and 5a). This indicates the significant impact of the tangential flow component on the interface shape.

The magnetic field appears to be acting to mix silicon away from the region near the crucible wall into the center, a direction inverse to the case with no applied field (Fig. 3d and 5d). This action creates a higher concentration gradient near the crucible wall at the edge of the silicon source, and increases dissolution (Fig. 5c). Thus, in both cases (with and without magnetic field) the melt flow gives rise to mixed and semi-mixed regions near the dissolution interface. Under the 0.8 Tesla magnetic field, much higher dissolution rates were realized at the edge of the source material, which is in agreement with the experimental observations (Fig. 9).

In the 3-D simulations, magnetic field levels under ($B_0 < 0.2$ Tesla) appear not to have a significant impact on the flow structure. For magnetic field levels in the range of ($0.2 \leq B_0 < 0.6$ Tesla), the applied field does not have significant effects on the flow structure nor on the interface shape but causes a non-uniform

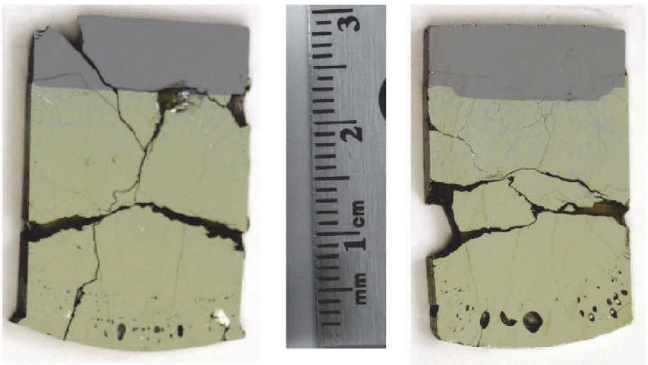

Figure 9: Polished cross-sections of the quenched samples from the experiments conducted with no field on the left and that with a 0.8 Tesla field on the right [Armour and Dost 2009]. On the left, we see that the silicon dissolution interface remains almost flat, but on the right, more silicon dissolved near the edge of the dissolution interface (curved area).

concentration distribution in the melt (Fig. 4b and 4c). Magnetic field levels in the range of ($0.6 \leq B_0 \leq 0.8$ Tesla), however, have a significant impact on the flow structure and lead to a more uniform concentration distribution in the melt (Figs. 5b and 5c).

Due to a small increase in the amount of dissolved silicon (Fig. 2), it appears that the ($0.2 \leq B_0 < 0.6$ Tesla) range of applied field does not have a significant impact on the flow structure. Particularly the 3-D simulation results well predict this observation. In the center region and near the crucible bottom, both the radial and tangential flow velocity components appear to be smoothed out and slightly damped (Figs. 6c, 6d, 7c and 7d). In the regions ahead of the dissolution interface near the crucible wall, however, these flow velocity components appear to be smoothed and slightly enhanced (Fig. 6c, 6d, 7c and 7d). Also, except the regions near to the wall, where the axial flow appears to be enhanced, the similar trend may be observed for the axial flow (Figs. 6e and 7e).

The effect of the 0.8 Tesla level of applied field on flow structures is significant as shown by the 3-D simulation. In the center region and near the crucible bottom, both the radial and tangential flow velocity components appear to be weakened and are inverted in direction (Figs. 6c, 6d, 8c and 8d). In the regions near the interface and close to the crucible wall, however, these two flow velocity components appear to get slightly stronger and are inverted (Figs. 6c, 6d, 8c and 8d). Furthermore, except the regions near to the crucible wall where the axial flow is stronger and inverted in direction (Figs. 6e and 8e), the axial flow velocity appears to be weakened (for instance at the positions z = 2 mm and 12 mm) and almost suppressed (for instance at z = 23 mm) in the rest of the domain. These observations were noted by [Armour and Dost (2009)].

In most crystal growth systems, a static magnetic field is frequently utilized to suppress thermosolutal convective fluid flow in the melt. In the present crucible configuration, however, it appears that the melt flow is not suppressed. Instead, the already weak stable flow structure is strengthened under the effect of applied magnetic field due to the buoyancy of the silicon solute. Indeed, the applied field strengthens and inverts the upward flow near to the crucible wall and weakens and inverts the downward flow in the center region and near the crucible bottom (Figs. 3 and 5).

In fact, an external magnetic field, aligned perfectly with the axis of the growth cell (z-direction), gives rise to a magnetic body force in the radial plane that balances the vertical gravitational body force, and consequently strengths both the radial and the tangential flow velocity components, and suppresses the axial flow. This fluid flow behavior can easily be understood from the fact that maximum electromagnetic damping of the fluid flow occurs when the velocity field $\mathbf{u}$ is oriented

orthogonal to the magnetic field vector $\mathbf{B} = B_0\mathbf{e}_z$ because of the particular form of the electromagnetic damping force ($\mathbf{F}_E = \sigma_e(\mathbf{u} \times \mathbf{B}) \times \mathbf{B}$). It should be noted that the axisymmetric model fails to predict these trends.

The present 3-D numerical simulation results confirm the experimental observations of [Armour and Dost (2009)]. The observed dissolution structure may be valuable to the LPD crystal growth of Si-Ge system, where the curvature of the growth interface evolves with time. It may be possible to use this effect to better control interface shape.

5 Conclusions

The numerical simulations conducted for the dissolution process of silicon into germanium melt using both axisymmetric and 3-D simulation domains led to the following conclusions.

-Transport of silicon in the Ge-rich melt where silicon is being dissolved from the top exhibits a diffusion-dominated behavior (in the region near to the dissolution interface and the center). This behavior is due to the silicon solute buoyancy in the heavier Ge-rich melt, which has been previously explained experimentally by [Armour and Dost (2009)] and predicted numerically by [Yildiz, Dost and Lent (2005)].

-The present 3-D simulation predicts that the application of a static magnetic field strengthens the radial and tangential flow velocity components in the region near the crucible wall at the edge of the silicon source, and thus leads to a stronger convective flow pattern in the melt close to this region. Consequently, this change in the melt flow gives rise to a significant mixing of silicon away from the region near the crucible wall into the center of the melt. This phenomenon may have an application in controlling growth interface geometry and maintaining a constant growth interface curvature during the LPD growth of SiGe single crystals.

-Axial mixing in the melt does not appear to significantly increase and the concentration profile seems to evolve in a diffusion-dominated manner.

-The chosen value of silicon diffusivity $D_L^{Si} = 2.5 \times 10^{-8} m^2/s$ agrees well with experiment.

-The numerical results of the present simulations indicate that the silicon dissolution was slightly enhanced under an applied vertical magnetic field. This enhancement peaked for the field levels between 0.2 to 0.5 Tesla. The magnetic level of 0.8 Tesla appears to be an optimum value for obtaining uniform concentration distribution. This observation can be attributed to the altered flow structure in the melt due to the applied magnetic field.

-Simulation results also show that, as the magnitude of the applied magnetic field increases, the flow pattern becomes *three-dimensional*. The radial and tangential flow velocity components increase, causing higher dissolution rates at the edge of the silicon source. These observations were well predicted by the 3-D model while the axisymmetric model failed to do so.

Acknowledgement: The financial support provided by the Natural Sciences and Engineering Research Council of Canada (NSERC) and the Canada Research Chairs (CRC) Program is gratefully acknowledged.

References

Armour, N.; Dost, S. (2009): Effect of an applied static magnetic field on silicon dissolution into a germanium melt. *Journal of Crystal Growth*, vol. 311, pp. 780–782.

Armour, N.; Dost, S.; Lent, B. (2007): Effect of free surface and gravity on silicon dissolution in germanium melt. *Journal of Crystal Growth*, vol. 299, pp. 227–233.

Armour, N.; Sheibani, H.; Dost, S. (2006): Growth of cadmium zinc telluride by liquid phase electroepitaxy. *Crystal Research and Technology,* vol. 41, no. 10, pp. 939–945.

Armour, N.; Yildiz, M.; Yildiz, E.; Dost, S. (2008): Liquid Phase Diffusion Growth of SiGe Single Crystals under Magnetic Fields. *ECS Transactions*, vol. 16, no. 10, pp. 135–146.

COMSOL Multiphysics Modeling Guide (2008): by COMSOL AB. Tegnérgatan 23 SE-111 40 Stockholm, Sweden.

Deal, A. (2004): *Enhanced morphological stability in Sb-doped Ge single crystals,* PhD thesis, Florida University, USA.

Donea, J.; Huerta A. (2003): *Finite Element Methods for Flow Problems.* John Wiley & Sons, Ltd.

Dost, S.; Lent, B. (2007): *Single Crystal Growth of Semiconductors from Metallic Solutions*. Elsevier, Amsterdam, the Netherlands.

Ed Akin, J.; Tezduyar, T.E. (2004): Calculation of the advective limit of the SUPG stabilization parameter for linear and higher-order elements. *Computer Methods in Applied Mechanics and Engineering*, vol. 193, pp. 1909–1922.

Förster C. (2007): *Robust methods for fluid-structure interaction with stabilized finite elements,* PhD thesis University of Stuttgart, Germany.

Franca, L.P.; Frey, S.L.; Hughes, T.J.R. (1992): Stabilized finite element methods: I. Application to the advective-diffusive model. *Computer Methods in Applied*

Mechanics and Engineering, vol. 95, pp. 253–276.

Giessler C., Sievert C., Krieger U., Halbedel B., Huelsenberg D., Luedke U., Thess A. (2005): A Model for Electromagnetic Control of Buoyancy Driven Convection in Glass Melts. *FDMP: Fluid Dynamics & Materials Processing,* vol.1, no.3, pp.247-266.

Gulluoglu, A.N.; Tsai, C.T. (2000): Effects of growth direction on twin formation in GaAs crystal grown by vertical gradient freeze method. *CMES: Computer Modeling in Engineering and Sciences,* vol. 1, no.1, pp. 85-89.

Hauke, G.; Hughes, T.J.R. (1998): A comparative study of different sets of variables for solving compressible and incompressible flows. *Computer Methods in Applied Mechanics and Engineering*, vol. 153, pp. 1–44.

Kakimoto, K.; Liu, L. (2006): Flow Instability of Silicon Melt in Magnetic Fields. *FDMP: Fluid Dynamics & Materials Processing*, vol.2, no.3, pp.167-173.

Kumar, V.; Dost, S.; Durst, F. (2007): Numerical modeling of crystal growth under strong magnetic fields: An application to the travelling heater method. *Applied Mathematical Modelling,* vol. 31, pp. 589–605.

Lappa, M., (2005): Review: Possible strategies for the control and stabilization of Marangoni flow in laterally heated floating zones. *FDMP: Fluid Dynamics & Materials Processing*, vol.1, no.2, pp. 171−−187.

Liu, Y. C.; Okano, Y.; Dost, S. (2002): The effect of applied magnetic field on flow structures in liquid phase electroepitaxy – a three dimensional simulation model. *Journal of Crystal Growth*, vol. 244, pp. 12–26.

Liu, Y. C.; Dost, S.; Lent, B.; Redden, R. F. (2003): A three-dimensional numerical simulation model for the growth of CdTe single crystals by the traveling heater method under magnetic field. *Journal of Crystal Growth*, vol. 254, pp. 285–297.

Mechighel, F. (2013): *Modélisation de la convection lors d'un changement de phase : Stabilisation par champ magnétique.* (editor Morel P.) Presses Académiques Francophones 'PAF', Saarbrücken, Germany.

Mechighel, F.; Armour, N.; Dost, S.; Kadja, M. (2011): Mathematical modeling of the dissolution process of silicon into germanium melt. *TWMS Journal of Applied and Engineering Mathematics (Turkic Word Mathematical Society),* vol.1, no.2, pp. 200–222.

Müller, G.; Ostrogorsky, A.G. (1994): *Convection in melt growth.* Chapter 13, Handbook of Crystal Growth. (editor Hurle D.T.J.), North-Holland/Elsevier, vol. 2, pp. 711−−814.

Okano, Y.; Nishino, S-S.; Ohkubo, S-S.; Dost, S. (2002): Numerical study of transport phenomena in the THM growth of compound semiconductor crystal.

Journal of Crystal Growth, vol. 238–239; pp. 1779–1784.

Polner, M. (2005): *Galerkin Least-Squares Stabilization Operators for the Navier-Stokes Equations: A Unified Approach,* PhD thesis University of Twente, AE Enschede, The Netherlands.

Saad, Y.; Schultz, M. H. (1986): GMRES: A generalized minimal residual algorithm for solving nonsymmetric linear systems. *SIAM Journal of Scientific and Statistical Computing,* vol. 7, no. 3, pp. 856–869.

Sampath, R.; Zabaras, N. (2001): Numerical study of convection in the directional solidification of a binary alloy driven by the combined action of buoyancy, surface tension, and electromagnetic forces. *Journal of Computational Physics,* vol. 168, pp. 384–411

Shakib, F. (1988): *Finite element analysis of the compressible Euler and Navier-Stokes equations*, Ph.D. Thesis, Department of Mechanical Engineering, Stanford University, Stanford, California.

Tezduyar, T. E. (1992): Stabilized Finite Element Formulations for Incompressible Flow Computations. *Advances in Applied Mechanics*, vol. 28, pp. 1–44.

Tezduyar, T. E.; Mittal, S.; Ray, S. E.; Shih, R. (1992): Incompressible flow computations with stabilized bilinear and linear equal-order-interpolation velocity-pressure elements'. *Computer Methods in Applied Mechanics and Engineering*, vol. 95, pp. 221–242.

Tezduyar, T. E.; Osawa, Y. (2000): Finite element stabilization parameters computed from element matrices and vectors. *Computer Methods in Applied Mechanics and Engineering*, vol. 190, pp. 411-430.

Yildiz, M. (2005): *A Combined Experimental and Modeling Study for the Growth of Si_xGe_{1-x} Single Crystals by Liquid Phase Diffusion (LPD)*, PhD thesis, University of Victoria, Canada.

Yildiz, E.; Dost, S. (2007a): A numerical simulation study for the combined effect of static and rotating magnetic fields in liquid phase diffusion growth of SiGe. *Journal of Crystal Growth,* vol. 303, pp. 279–283.

Yildiz, M.; Dost, S. (2005): A continuum model for the Liquid Phase Diffusion growth of bulk SiGe single crystals. *International Journal of Engineering Science,* vol. 43, pp. 1059–1080.

Yildiz, M.; Dost, S. (2007b): Incorporation of surface tension to interface energy balance in crystal growth. *Crystal Research and Technology,* vol. 42, no. 9, pp. 914–919

Yildiz, M.; Dost, S.; Lent, B. (2005): Growth of bulk SiGe single crystals by liquid phase diffusion. *Journal of Crystal Growth,* vol. 280, pp. 151–160

Yildiz, M.; Dost, S.; Lent, B. (2006): Evolution of the growth interface in liquid phase diffusion growth of bulk SiGe single crystals. *Crystal Research and Technology,* vol. 41, no. 3, pp. 211 –216.

Yildiz, E.; Dost, S.; Yildiz, M. (2006): A numerical simulation study for the effect of magnetic fields in liquid phase diffusion growth of SiGe single crystals. *Journal of Crystal Growth,* vol. 291, pp. 497–511.